Applied Physics A (2024) 130:428
https://doi.org/10.1007/s00339-024-07589-2

# Terahertz metasurfaces to demonstrate an extremely wide range of refractive indices in the 0.3-THz band

Kento Sato[1] · Kazuhisa Watai[1] · Koki Ishihara[2] · Ryuji Ohuchi[2] · Satoshi Kondoh[1] · Tatsuya Sato[2] · Takehito Suzuki[3]

Received: 17 August 2023 / Accepted: 12 May 2024 / Published online: 21 May 2024
© The Author(s), under exclusive licence to Springer-Verlag GmbH Germany, part of Springer Nature 2024

## Abstract

Metasurfaces suitable for the terahertz gap are alternatives to naturally occurring materials and could accelerate the development of terahertz flat optics integrated with terahertz continuous-wave sources. However, metasurfaces have yet to be commonly adopted in terahertz devices that require a number of specific material properties because of the many choices in meta-atom design. In this paper, we demonstrate that simple dimension control of a single kind of meta-atom enables the design of a wide range of refractive indices from large positive to negative values in the 0.3-THz band. Measurements by terahertz time-domain spectroscopy verify three kinds of metasurfaces with (1) an extremely high refractive index of $12.3+j0.88$ and reflectance of 5.1% at 0.31 THz, (2) a zero refractive index of $-0.44+j0.12$ and reflectance of 2.6% at 0.34 THz, and (3) a negative refractive index of $-5.4+j0.32$ and reflectance of 22.7% at 0.31 THz. The 0.3-THz band is a frequency band for candidates to 6G wireless communications. Our results offer an accessible material platform for terahertz flat optics such as metalenses, antennas, and phase plates. Terahertz flat optics based on our presented metasurfaces would be a welcome contribution to the development of terahertz industries, including 6G wireless communications.

**Keywords** Metasurface · Metamaterial · High refractive index · Zero refractive index · Negative refractive index

## 1 Introduction

Manipulating terahertz waves is a key to developing emerging terahertz industrial applications such as 6G wireless communications [1–4], imaging [5–7], and security [8]. Devices in terahertz industrial applications could contain continuous-wave (CW) sources radiating terahertz waves. Terahertz CW sources have developed rapidly to include resonant tunneling diodes (RTD) [9], quantum cascade lasers (QCL) [10], and Gunn diodes [11], to fulfill the commonly called terahertz gap. Terahertz waves radiated from terahertz CW sources pass through optical components to produce wavefronts including collimating [12, 13], focusing [14–16], circularly polarized waves [17], and optical vortices [18–20]. Many optical components manipulating terahertz waves are frequently made of naturally occurring materials such as cyclo-olefin polymer (COP) with a refractive index of 1.54 [21], magnesium oxide (MgO) 3.1 [22], and silicon (Si) 3.4 [23] in the terahertz waveband. However, three-dimensional bulky optical components made of naturally occurring materials are designed based on materials offering limited choices of refractive indices. Further, naturally occurring materials in the terahertz waveband commonly have the relative permeability fixed at 1.0 and are subject to high Fresnel reflections.

Metasurfaces enable the design of a wide range of refractive indices due to the simultaneous control of both relative permittivity and relative permeability. Flat optics based on metasurfaces makes it possible to replace frequently used three-dimensional bulky optical components with two-dimensional planar optical components [24–28]. The design of refractive indices, distribution, and polarization

✉ Takehito Suzuki
takehito@go.tuat.ac.jp

1 Department of Electrical and Electronic Engineering, Graduate School of Engineering, Tokyo University of Agriculture and Technology, 2-24-16 Naka-cho, Koganei-shi, Tokyo 184-8588, Japan

2 Department of Electrical and Electronic Engineering, Graduate School of Engineering, Ibaraki University, 4-12-1 Nakanarusawa-cho, Hitachi, Ibaraki 316-8511, Japan

3 Division of Advanced Electrical and Electronics Engineering, Institute of Engineering, Tokyo University of Agriculture and Technology, 2-24-16 Naka-cho, Koganei-shi, Tokyo 184-8588, Japan

properties of the metasurfaces enables the development of two-dimensional planar optical components such as collimating [29, 30], focusing [31–33], optical vortices [34], polarization conversion [35, 36], beam steering [37], and beam splitter [38, 39]. Our previous work in [29] has experimentally demonstrated a gradient-refractive-index collimating metalens made with our original metasurface with an extremely high refractive index and low reflectance [40]. The two-dimensional planar collimating metalens has a sharp gradient of refractive indices distributed from the center to the periphery. The collimating metalens converts terahertz waves radiated from an RTD to plane waves with high directivity. Further, a metalens is mounted on an RTD with the short focal distance of 1 mm (1 λ) [30]. Simulations have verified a focusing metalens [33] made with a negative refractive index [41]. Metasurfaces with high [40, 42–46]; zero [47, 48]; and negative refractive indices [41, 49–56] have been reported with different meta-atoms, frequency bands, and fabrication methods all helping to accelerate the development of terahertz flat optics [29–39]. Metasurfaces with a wide range of refractive indices consisting of rectangular meta-atoms at the same frequency would be a welcome contribution to enable an accessible platform for terahertz flat optics.

This paper aims to develop materials with on-demand optical constants to accelerate the growth of terahertz industrial applications. In this paper, we show that rectangular meta-atoms with different dimensions make it possible to design low-reflection metasurfaces with an extremely high refractive index above 10, a zero refractive index, and a negative index below 0 [57]. The material properties are produced by the control of the relative permeability as well as the permittivity. This is in contrast to the permeability of naturally occurring materials which cannot commonly be controlled in the terahertz waveband. The metasurfaces consist of cut metal wires symmetrically aligned on the front and back of a dielectric substrate. The operating frequency is the 0.3-THz band, a candidate frequency band for 6G wireless communications. Measurements by terahertz time-domain spectroscopy (THz-TDS) verify the three kinds of metasurfaces with an extremely high refractive index of $12.3+j0.88$ and low reflectance of 5.1% at 0.31 THz, a zero refractive index of $-0.44+j0.12$ and low reflectance of 2.6% at 0.34 THz, and a negative refractive index of $-5.4+j0.32$ and low reflectance of 22.7% at 0.31 THz. These metasurfaces with a wide range of refractive indices would provide an accessible platform for terahertz flat optics. Terahertz flat optics based on the metasurfaces would offer attractive components such as high numerical aperture metalenses, high directivity antennas, and optical vortex phase plates.

## 2 Metasurfaces with an extremely wide range of refractive indices in the 0.3-THz band

Figure 1(a)–(c) illustrate metasurfaces with extremely high, zero, and negative refractive indices at 0.3-THz, respectively. Figure 1(d) shows an enlarged view of the metasurface with an extremely high refractive index. The metasurfaces consist of symmetrically aligned paired cut metal wires on the front and back of a dielectric substrate. The meta-atoms of the cut metal wires allow more design freedom than those of the square metal patches [58]. The length of the cut metal wires, the gap along the $y$-axis, the thickness of the dielectric substrate, the distance between the cut metal wires along the $x$-axis, the width of the cut metal wires, and the thickness of the cut metal wires are $g$, $l$, $d$, $s$, $w$, and $t$, respectively. The meta-atoms of the cut metal wires have the six parameters of $g$, $l$, $d$, $s$, $w$, and $t$. The meta-atoms of the square metal patches have the four parameters of $l$, $d$, $s$, and $t$. The design freedom of the cut metal wires would offer a wide range of refractive indices, maintaining low reflectance.

The double-sided cut metal wires on the front and back of a dielectric substrate control the relative permittivity $\varepsilon_r$ and permeability $\mu_r$ of the metasurfaces. The refractive index and relative impedance of the metasurfaces are expressed as $n=\sqrt{\epsilon_r\mu_r}$ and $Z_r=\sqrt{\mu_r/\epsilon_r}$, respectively. The metasurface with an extremely high refractive index and low reflectance in Fig. 1(a) has the relative permittivity $\varepsilon_r$ and permeability $\mu_r$ with high values. The metasurface with a zero refractive index and low reflectance in Fig. 1 (b) has the relative permittivity $\varepsilon_r$ and permeability $\mu_r$ with zero values. The metasurface with a negative refractive index and low reflectance in Fig. 1(c) has the relative permittivity $\varepsilon_r$ and permeability $\mu_r$ with negative values. The simultaneous control of the relative permittivity and permeability with high, zero, and negative values at the same frequency make it possible to design extremely high, zero, and negative refractive indices, respectively. The control of the relative permittivity $\varepsilon_r$ and permeability $\mu_r$ with similar values at the same frequency can also produce low reflection characteristics because the Fresnel reflections is reduced due to impedance matching as in circuit theory.

Tables 1, 2, and 3 give an overview of the reported high, zero, and negative refractive index metasurfaces, respectively. To the best of our knowledge, this is the only work that has demonstrated, by measurements, that simple dimensional control of a single kind of meta-atoms enables the design of a wide range of refractive indices from extremely high to negative values in the 0.3-THz band.

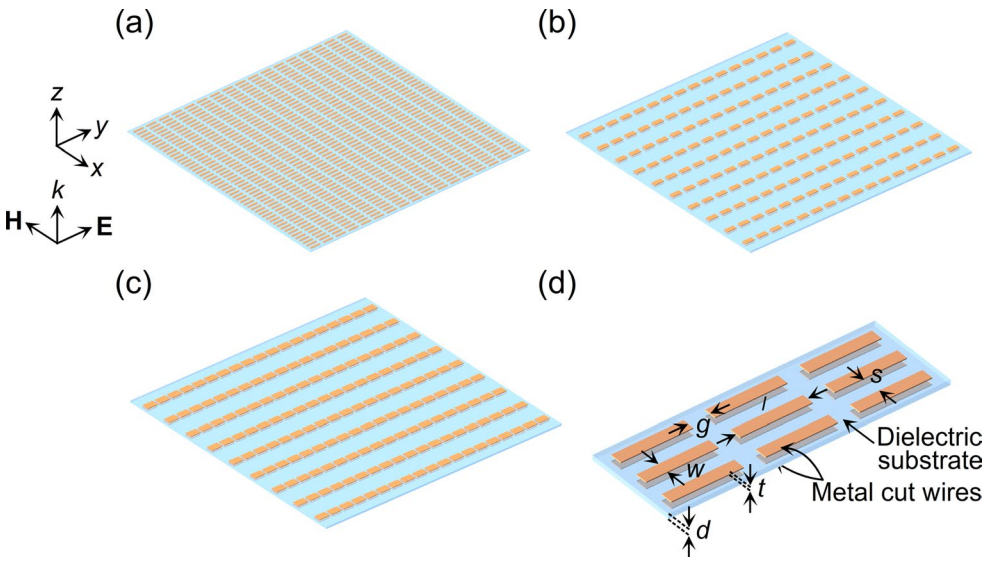


**Fig. 1** Metasurfaces of symmetrically aligned paired cut metal wires on the front and back of a dielectric substrate with (**a**) an extremely high refractive index, (**b**) a zero refractive index, and (**c**) a negative refractive index. (**d**) The meta-atoms of the metasurface with an extremely high refractive index

**Table 1** Measured and simulated material characteristics of high refractive index metasurfaces

| Year | f (THz) | Structure of meta-atoms | *n* | *R* (%) | T (%) | |
|---|---|---|---|---|---|---|
| 2011 | 0.522 | I-shaped metal patches | 24.34 | - | - | [42] |
| 2013 | 0.48 | I-shaped metal patches | 18.4 | - | < 10 | [43] |
| 2015 | 0.315 | Z-shaped metal patches | 14.36 | > 90* | < 10 | [44] |
| 2017 | 0.309 | Double-sided paired cut metal wires | 6.66 | 1.16 | 91.8 | [40] |
| 2017 | 0.827 | Double-sided window-type metal wires | 6.8* | 5* | 42* | [45] |
| 2021 | 2.97 | Double-sided paired cut metal wires | 5.88 | 1.3 | 35.7 | [46] |
| 2024 | 0.31 | Double-sided paired cut metal wires | 12.3 | 5.1 | 73.1 | This work |

**Table 2** Measured and simulated material characteristics of zero refractive index metasurfaces

| Year | f (THz) | Structure of meta-atoms | *n* | *R* (%) | T (%) | |
|---|---|---|---|---|---|---|
| 2014 | 0.522 | Double-sided metal fishnets | -0.307* | - | - | [47] |
| 2020 | 0.5 | Double-sided paired cut metal wires | 0.16 | 0.7 | 97.3 | [48] |
| 2024 | 0.34 | Double-sided paired cut metal wires | -0.44 | 0.7 | 97.3 | This work |

**Table 3** Measured and simulated material characteristics of negative refractive index metasurfaces

| Year | f (THz) | Structure of meta-atoms | *n* | *R* (%) | T (%) | |
|---|---|---|---|---|---|---|
| 2008 | 0.458 | I-shaped metal patches | -2.74 | - | - | [49] |
| 2008 | 1.02 | Cross shaped metal patches | -1.81* | - | - | [50] |
| 2008 | 2.64* | Double-sided rectangular metal patches | -11.7* | 14.7* | 88.3* | [52] |
| 2008 | 2.22 | S-shaped gold strings | - | - | - | [53] |
| 2009 | 1.3 | I-shaped metal patches | -1.7* | - | - | [51] |
| 2009 | 0.69 | Double-sided window-type metal wires | -2.8 | 75.8* | - | [54] |
| 2013 | 0.373 | Dielectric cube array | -4.37 | 68.3* | 4.0* | [55] |
| 2013 | 0.55 | Double-sided metal fishnets | -15 | 98.8 | 23.1 | [56] |
| 2014 | 0.31 | Metal fish net | -4.47 | 94.4* | 4.68* | [47] |
| 2018 | 0.42 | Double-sided paired cut metal wires | -4.2 | 4.3 | 81.5 | [41] |
| 2024 | 0.31 | Double-sided paired cut metal wires | -5.4 | 22.7 | 56.4 | This work |

The *n*, *R*, and *T* represent the refractive index, reflectance, and transmittance, respectively

*Asterisks denote values obtained through simulations

## 3 Design of the metasurfaces

Figure 2(a) and (b) illustrate equivalent circuits that explain the operating principle of the metasurfaces. Equivalent circuit theory approximately explains the dielectric and magnetic properties of the metasurfaces. The control of the length $l$ and the gap $g$ of the cut metal wires determines the dielectric and magnetic properties. The dielectric property arises from the electric field of the incident terahertz waves. The electric field of the incident terahertz waves generates currents on the cut metal wires of the front and back of the dielectric substrate in the same direction, resulting in the formation of serial resonance circuits. The resonance frequency of the dielectric property is determined by the inductance components $L_E$ of the cut metal wires and the capacitance components $C_E$ of the gaps between the cut metal wires along the $y$-axis. The magnetic property arises from the magnetic field of the incident terahertz waves. The magnetic field of the incident terahertz waves generates a current on the cut metal wires of the front and back of the dielectric substrate in the opposite direction, resulting in parallel resonance circuits. The resonance frequency of the magnetic property is determined by the inductance components $L_H$ of the cut metal wires and the capacitance components $C_H$ of the gaps between cut metal wires on the front and back of the dielectric substrate.

Figures 3, 4, and 5 show contour maps of the real part of the refractive indices, reflectance, transmittance relative permittivity, relative permeability, and relative impedance for the metasurfaces with extremely high, zero, and negative refractive indices, respectively. Table 4 shows the parameters

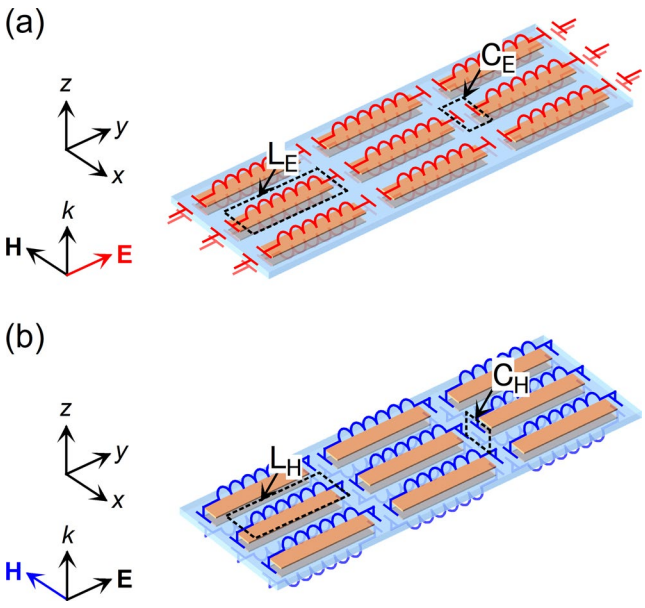


**Fig. 2** Equivalent circuits of symmetrically aligned paired cut metal wires on the front and back of a dielectric substrate with (**a**) dielectric and (**b**) magnetic properties

$g$, $l$, $d$, $s$, $w$, and $t$ of the fabricated metasurfaces with (a) extremely high, (b) zero, and (c) negative refractive indices, respectively. The contour maps in Figs. 3, 4, and 5 show the optical constants with varying gaps $g$ between the cut metal wires along the $y$-axis from 50 to 150 μm and lengths $l$ from 250 to 350 μm, respectively. The other parameters of distance $s$ between the cut metal wires along the $x$-axis, width $w$ of the cut metal wires along the $x$-axis, and the thickness $t$ of the cut metal wires are fixed in Table 4. When the length $l$ of the cut metal wire is changed, the adjacent cut metal wires are moved along the $+y$ or $-y$ direction. The gap $g$ is kept constant when changing the length $l$. The black dots in Figs. 3, 4, and 5 show the parameters of the fabricated metasurfaces described in Table 4. The optical constants of the metasurfaces are derived from scattering matrices $S_{11}$ and $S_{21}$ calculated by a finite element method simulator ANSYS HFSS [59]. The dielectric substrate is cyclo-olefin polymer (COP) with low loss properties and a refractive index of $1.53+j0.001$ [60] measured in the terahertz waveband. The metal of the cut metal wires is copper with a conductivity of $5.8\times10^7$ S/m. Copper can be used for metasurfaces [40, 41, 48, 57, 58] and antennas [29, 30] in the terahertz waveband. The complex conductivity of copper with the Drude model is $5.8\times10^7+2.7\times10^6$ S/m [46], and the real part of the conductivity is larger than the imaginary part.

Figure 3 shows the parameters of a metasurface with an extremely high refractive index $n_{\mathrm{eff}}$ of $12.2+j1.5$, a low reflectance of 70%, and transmittance of 65.1% for cut metal wires with $l=313$ μm and $g=94$ μm. The material property with a high refractive index of 12.2 is produced by the simultaneous control of the relative permittivity and relative permeability with high values. The relative permittivity $\varepsilon_r$ and permeability $\mu_r$ are $13.0-j1.5$ and $10.8+j4.1$, respectively, at 0.31 THz. The relative impedance $Z_r$ is $0.91+j0.22$. Figure 4 shows the parameters of a metasurface with a near-zero refractive index $n_{\mathrm{eff}}$ of $0.43+j0.009$, low reflectance of 2.0%, and high transmittance of 97.4% for cut metal wires with $l=318$ μm and $g=60$ μm. The material property with a near-zero refractive index of 0.43 is produced by the simultaneous control of the relative permittivity and relative permeability from 0 to 1.0. The relative permittivity and permeability are $0.87+j0.009$ and $0.21+j0.007$, respectively, at 0.31 THz. The relative impedance $Z_r$ is $0.49+j0.006$. Figure 5 shows the parameters of a metasurface with a negative refractive index $n_{\mathrm{eff}}$ of $-4.6+j0.16$, reflectance of 53.7%, and transmittance of 37.6% for cut metal wires with of $l=307$ μm and $g=136$ μm. The material property with a negative refractive index of $-4.6$ is produced by the simultaneous control of the relative permittivity and relative permeability below 0. The relative permittivity and permeability are $-12.9-j0.10$ and $-1.6+j0.12$, respectively, at 0.34 THz. The relative impedance $Z_r$ is $0.35-j0.01$.

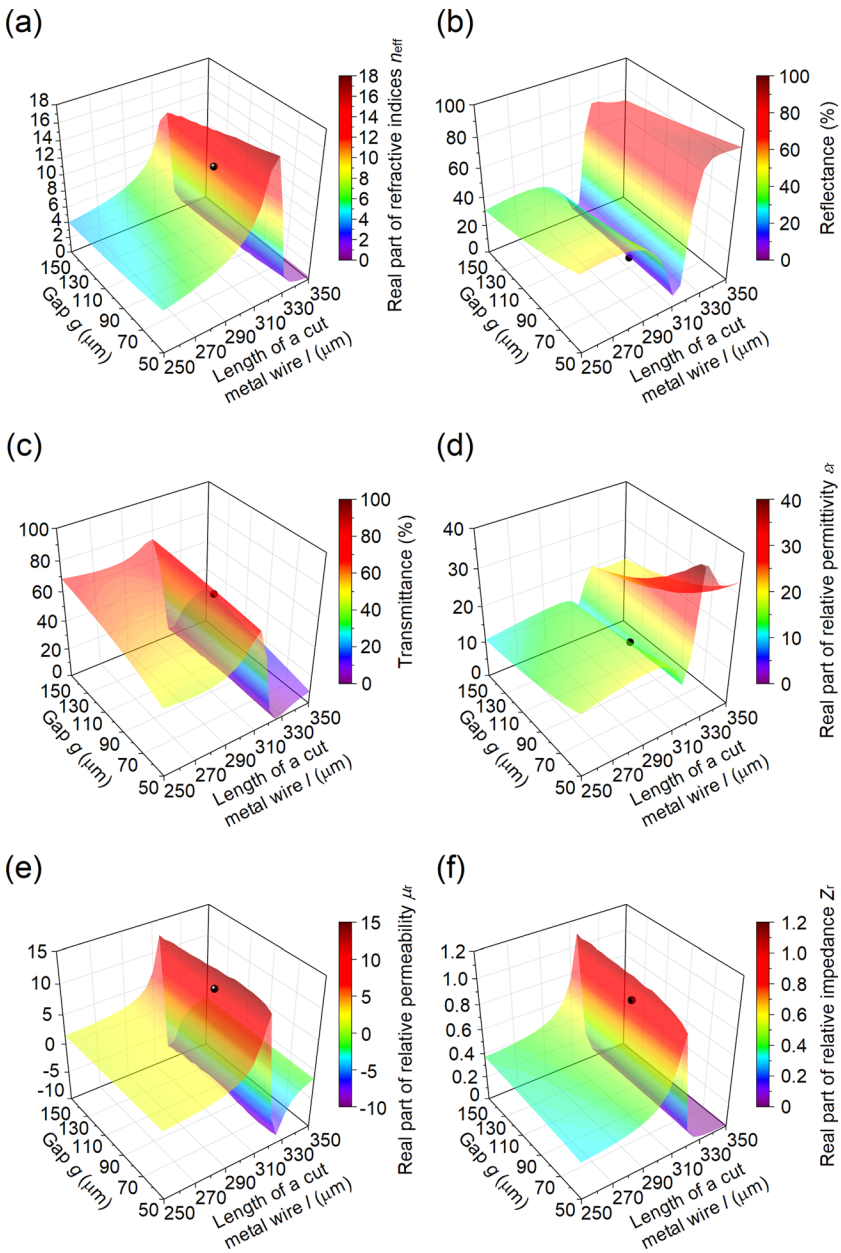


**Fig. 3** Contour maps for (**a**) the real part of the refractive indices $n_{eff}$, (**b**) reflectance, (**c**) transmittance, (**d**) the real part of the relative permittivity $\varepsilon_r$, (**e**) the real part of the relative permeability $\mu_r$, and (**f**) the relative impedance $Z_r$. Dots on the contour maps show the parameters of the fabricated metasurface with an extremely high refractive index of $12.2+j1.5$ at 0.31 THz

## 4 Fabrication and measurement of the metasurfaces

Figure 6 (a) shows a photograph of a fabricated metasurface with an extremely high refractive index. Figures 6 (b)–(d) show microscope images of fabricated meta-atoms composing the metasurfaces with extremely high, zero, and negative refractive indices, respectively. The dimensions of the metasurfaces are $40\times40$ mm$^2$. The metasurfaces with extremely high, zero, and negative refractive indices consist of 27,420, 5,349, and 5,088 pairs of double-sided cut metal wires. Cyclo-olefin polymer films coated with copper layers on the front and back are etched to fabricate the metasurfaces. The copper layers are coated without adhesive layers to reduce conductor losses in the metasurfaces.

Figure 7 (a) and (b) are photographs of the optical system for the measurements of transmittance and reflectance of the fabricated metasurfaces. Measurements by terahertz time-domain spectroscopy (THz-TDS) with TOPTICA Photonics TeraFlash verify the transmittance and reflectance of the fabricated metasurfaces and reference. The references of the transmittance and reflectance measurements are dry air and a silver mirror, respectively. The ratio of frequency characteristics of a metasurface to those of a reference in transmittance and reflectance measurements derives scattering matrices and calculates optical constants of the

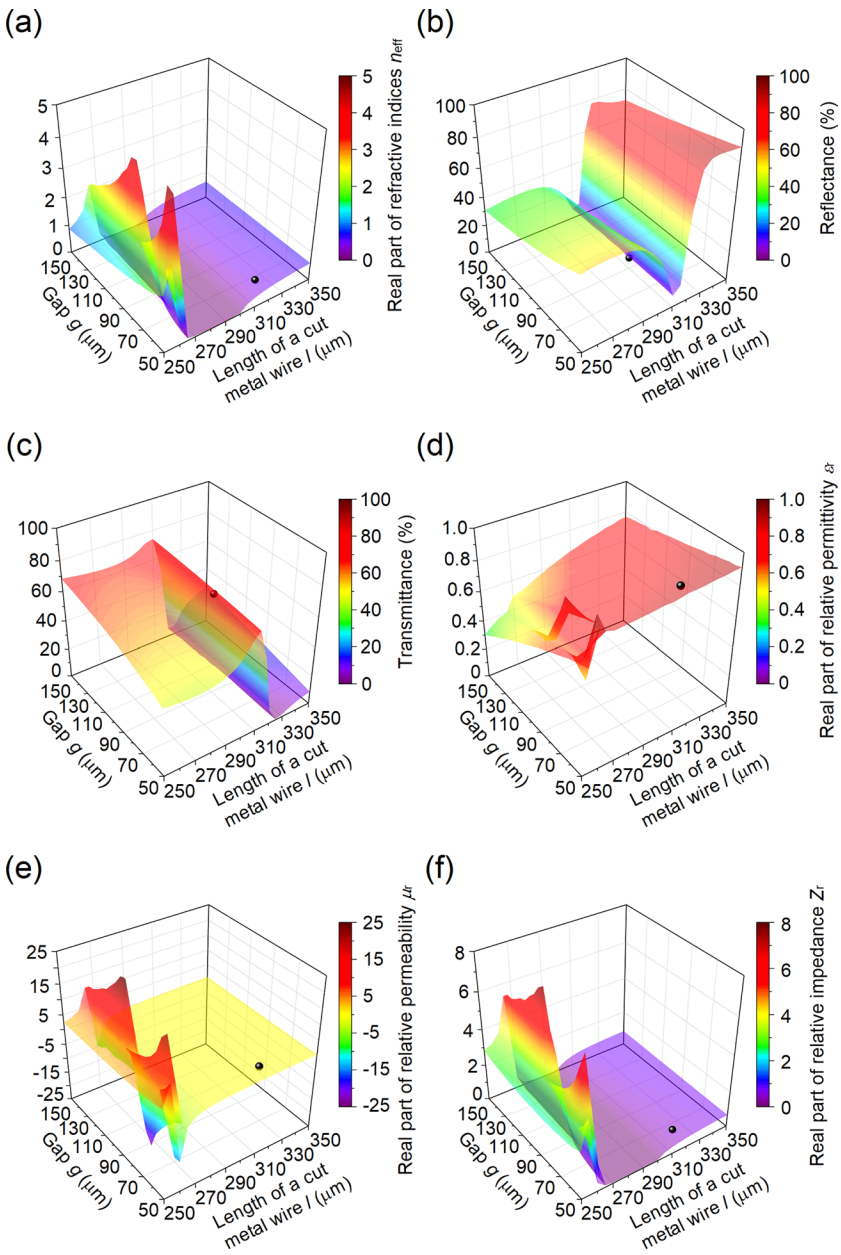


**Fig. 4** Contour maps for (**a**) the real part of the refractive indices $n_{eff}$, (**b**) reflectance, (**c**) transmittance, (**d**) the real part of the relative permittivity $\varepsilon_r$, (**e**) the real part of the relative permeability $\mu_r$, and (**f**) the relative impedance $Z_r$. Dots on the contour maps show the parameters of the fabricated metasurface with a zero refractive index of $0.43 + j0.009$ at 0.34 THz

metasurfaces such as refractive indices, relative permittivity, and permeability [59].

The main points of the measurement procedure are as follows. Pulsed terahertz waves are focused at the metasurfaces and silver mirror in transmittance and reflectance measurements. The calculated spot diameter and focal depth in the transmittance measurements are 3.5 and 19.6 mm, respectively. The calculated spot diameter and focal depth in the reflectance measurements are 7.1 and 78.5 mm. The optical lengths from the transmitted to the received photoconductive antennas are 419 and 698 mm in the transmittance and reflectance measurements, respectively. The fabricated metasurfaces are often deflected during the fabrication process. The deflection causes a difference in the position of the metasurfaces and the reference mirror in the reflectance measurements. The differences in optical lengths result in experimental errors. The metasurfaces have to be put in the same position as the reference mirror in the reflectance measurements to obtain accurate optical constants. The measured phases of the reflectance are compensated on the condition that the frequency characteristics of the measured phases are the same as those of the simulated phases. The compensation predicts that the metasurfaces with extremely high, zero, and negative refractive indices are concave with depths of 30, 7.5, and 45 μm along the incident terahertz waves, respectively.

Figure 8 (a)–(e), 9 (a)–(e), and 10 (a)–(e) show measurements of the material properties of the metasurfaces with an

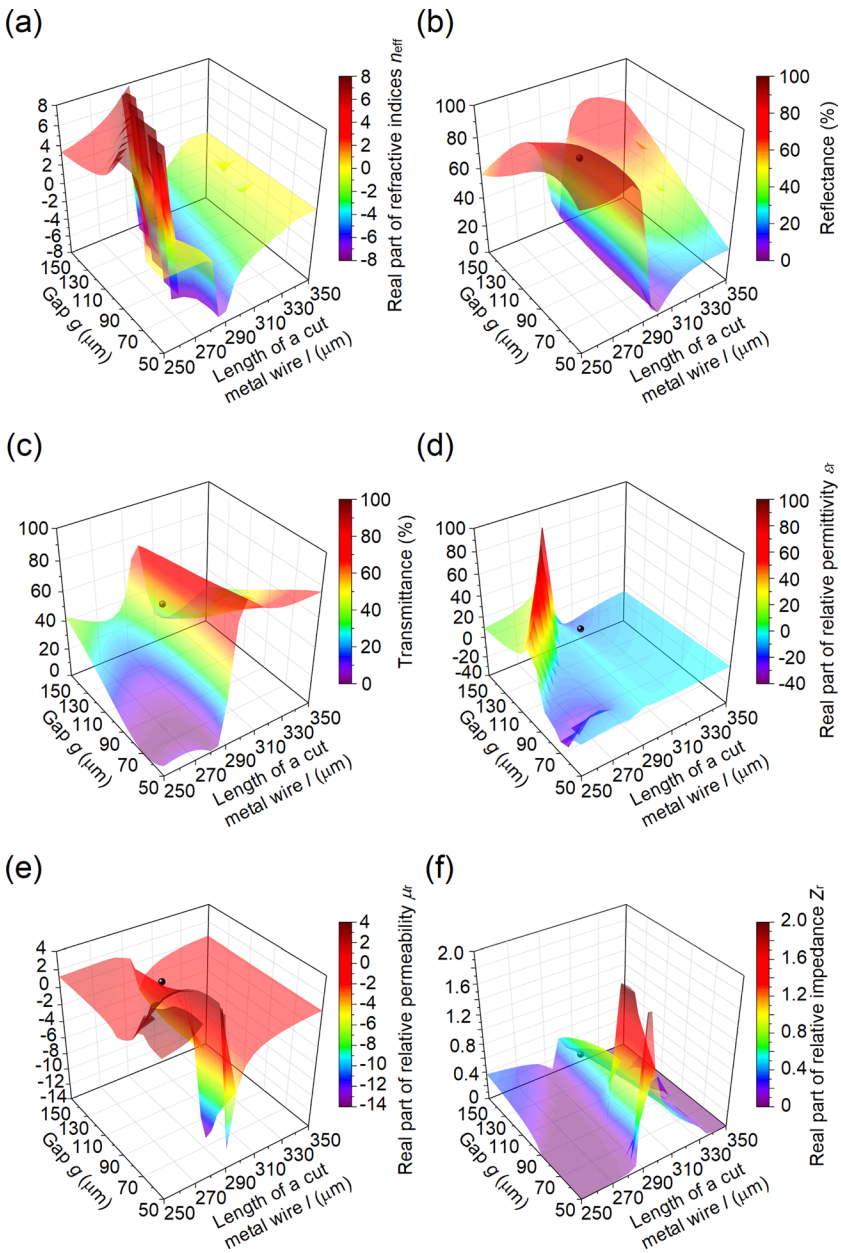


**Fig. 5** Contour maps for (**a**) the real part of the refractive indices $n_{eff}$, (**b**) reflectance, (**c**) transmittance, (**d**) the real part of the relative permittivity $\varepsilon_r$, (**e**) the real part of the relative permeability $\mu_r$, and (**f**) the relative impedance $Z_r$. Dots on the contour maps show the parameters of the fabricated metasurface with a negative refractive index of -4.6 + *j*0.16 at 0.31 THz

**Table 4** Parameters of the designed metasurfaces with (a) an extremely high refractive index at 0.31 THz, (b) a zero refractive index at 0.34 THz, and a negative refractive index at 0.31 THz

| | g (mm) | l (mm) | d (mm) | s (mm) | w (mm) | t (mm) |
|---|---|---|---|---|---|---|
| (a) | 94 | 313 | 23 | 86 | 54 | 0.5 |
| (b) | 60 | 318 | 50 | 597 | 208 | 6 |
| (c) | 136 | 307 | 50 | 557 | 149 | 6 |

extremely high refractive index, a zero refractive index, and a negative refractive index, respectively. The dots and solid lines in Figs. 8, 9, and 10 show measurements and simulations, respectively. Figure 8 (a)–(c) show that measurements verify that the fabricated metasurface with an extremely high refractive index has a refractive index of 12.3 + *j*0.88, low reflectance of 5.1%, and high transmittance of 73.1% at 0.31 THz. The relative permittivity, permeability, and impedance are 15.5 − *j*1.4, 9.6 + *j*2.3, and 0.79 + *j*0.13, respectively, at 0.31 THz. Figure 9 (a)–(c) show that the measurements verify that a fabricated metasurface with a zero refractive index has a refractive index of − 0.44 + *j*0.12, low reflectance of 2.6%, and high transmittance of 94.6% at 0.34 THz. The relative permittivity, permeability, and impedance are

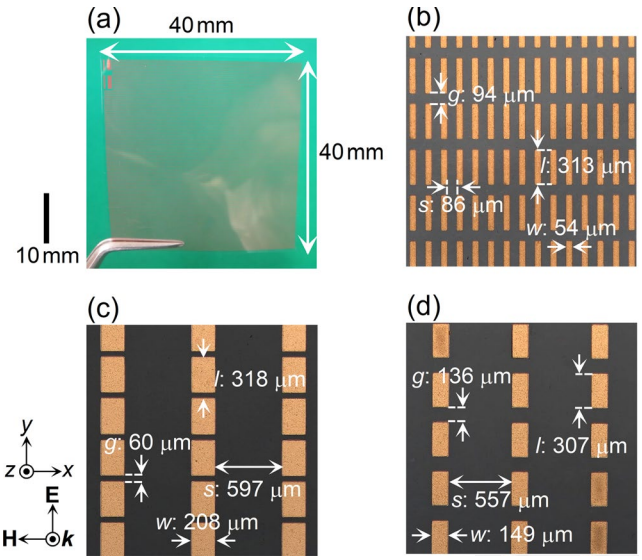


**Fig. 6** (**a**) Photographs of the fabricated metasurfaces with an extremely high refractive index. Laser microscopic image of the fabricated metasurfaces with (**b**) extremely high, (**c**) near-zero, and (**d**) negative refractive indices

$-0.19+j0.12$, $-0.93-j0.05$, and $1.9-j0.63$, respectively, at 0.34 THz. Figure 10 (a)–(c) show that measurements verify that a fabricated metasurface with a negative refractive index has a refractive index of $-5.4+j0.32$, low reflectance of 22.7%, and high transmittance of 56.4% at 0.31 THz. The relative permittivity, permeability, and impedance are $-9.7-j2.9$, $-2.6+j1.1$, and $0.5-j0.18$, respectively, at 0.31 THz.

## 5 Discussion of the metasurfaces

Figures 11, 12, and 13 show the measured dielectric energy loss, magnetic energy loss, and the sum of the dielectric energy and magnetic energy losses in the metasurfaces with extremely high, zero, and negative refractive indices, respectively. The energy loss in the metasurfaces is derived by the following equation [61].

$$Q = \frac{\omega\epsilon_0|E|^2}{2|\mu_r|}\left[|\mu_r|\,\mathrm{Im}\,(\epsilon_r) + |\epsilon_r|\,\mathrm{Im}\,(\mu_r)\right] \quad (1)$$

Here $\omega$ is the angular frequency, E is the electric field, and $\varepsilon_0$ is the permittivity in vacuum. The terms of the dielectric energy and magnetic energy losses are $|\mu_r|\,\mathrm{Im}\,(\epsilon_r)$ and $|\epsilon_r|\,\mathrm{Im}\,(\mu_r)$, respectively. The energy is absorbed in the metasurfaces when the sum of the dielectric energy and magnetic energy losses is positive also when the dielectric energy loss or magnetic energy loss is negative. Figures 11, 12, and 13 show that the measurements are very similar to the simulations, while the sum of the dielectric energy loss and magnetic energy loss is negative at a few frequencies. The regions highlighted with gray in Figs. 11, 12, and 13 show the frequency bands where the conservation of energy in the measurements is not satisfied due to measurement errors. The sum of the dielectric energy and magnetic energy losses calculated from the simulations are always positive from 0.25 to 0.35 THz. The simulations show that the energy is not amplified in the metasurfaces. The errors between the measurements and simulations would be caused by experimental errors.

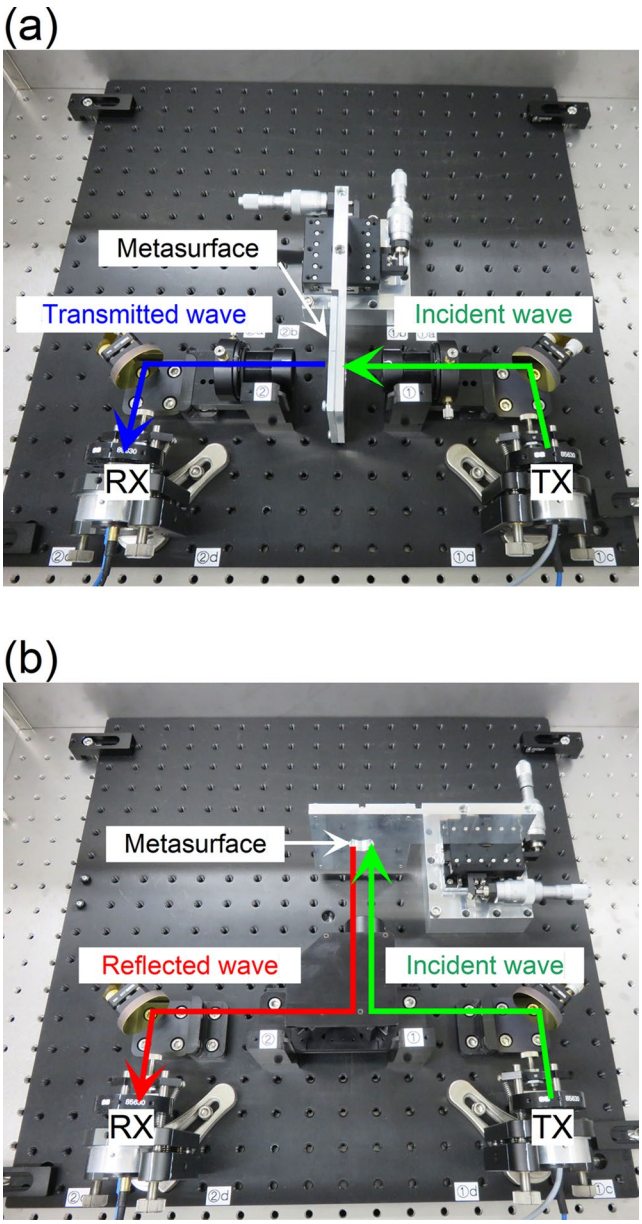


**Fig. 7** Optical system of the (**a**) transmittance and (**b**) reflectance measurements for the fabricated metasurfaces

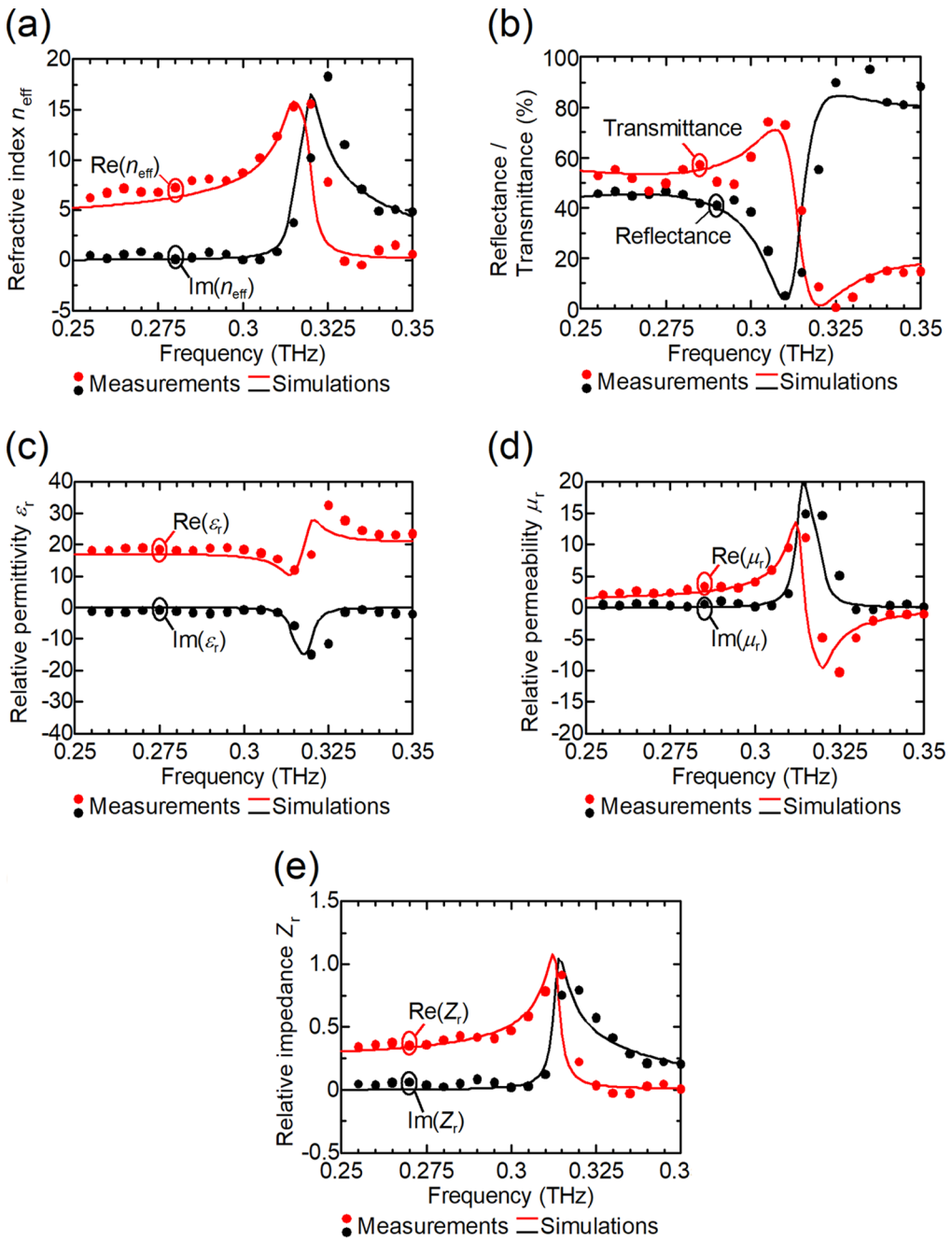


**Fig. 8** Frequency characteristics of (**a**) refractive index, (**b**) reflectance and transmittance, (**c**) relative permittivity, (**d**) relative permeability, and (**e**) relative impedance for metasurfaces with an extremely high refractive index

## 6 Conclusions

Metasurfaces consisting of double-sided paired cut metal wires make it possible to design a wide range of refractive indices including high, zero, and negative refractive indices. The simultaneous control of the relative permittivity and relative permeability with high, zero, and negative values at the same frequencies allow the design of extremely high, zero, and negative refractive indices. The control of the relative permittivity and permittivity with similar values reduces the Fresnel reflections. Measurements by THz-TDS verified the metasurfaces with an extremely high refractive index of 12.3 and low reflectance of 5.1%; a zero refractive index of − 0.44 and low reflectance of 2.6%; and a negative index of 5.4 and reflectance of 22.7% in the 0.3-THz band. The measurements presented here show that the parameter design of the cut metal wires enables a wide range of refractive indices: extremely high, zero, and negative. The

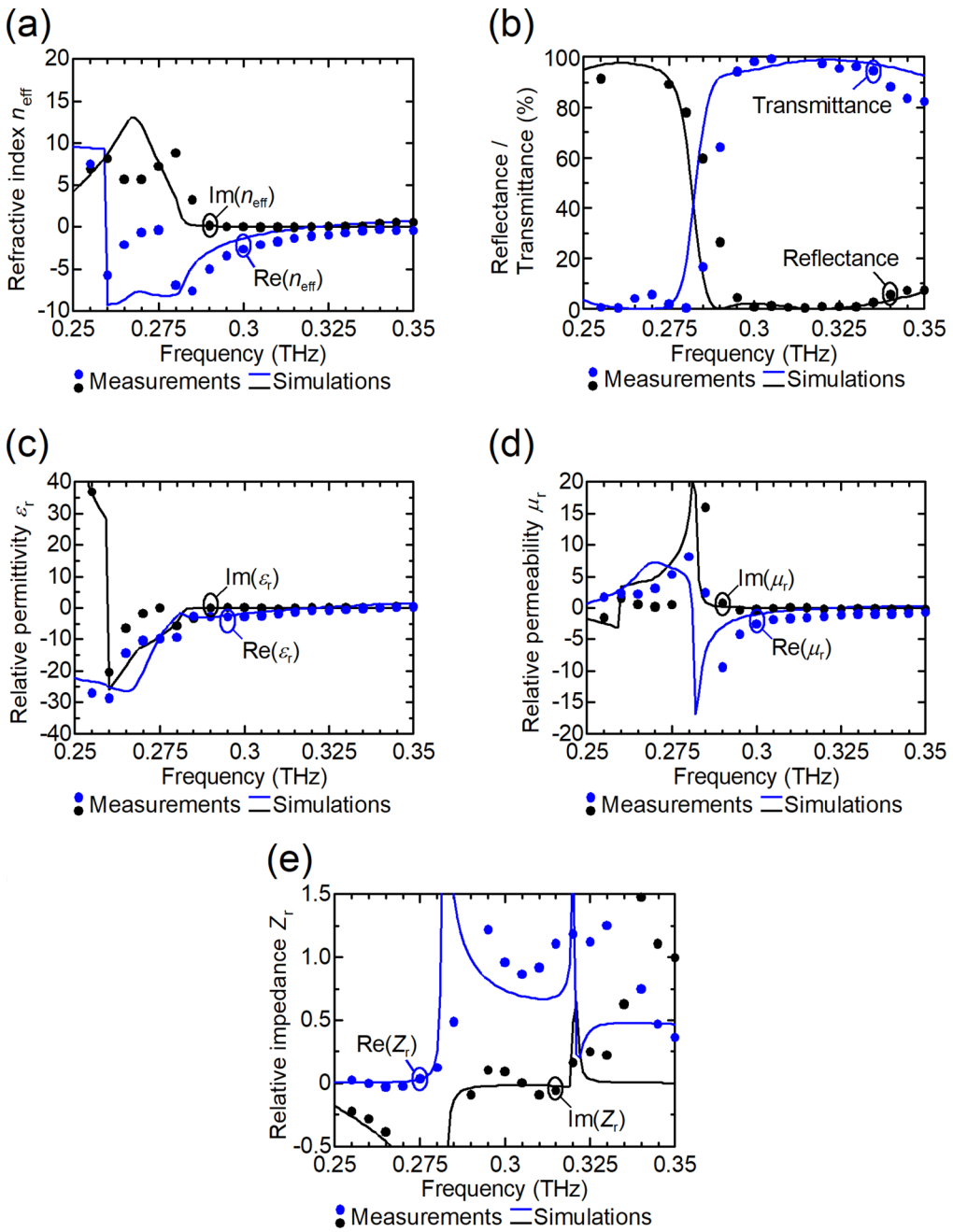


**Fig. 9** Frequency characteristics of (**a**) refractive index, (**b**) reflectance and transmittance, (**c**) relative permittivity, (**d**) relative permeability, and (**e**) relative impedance for metasurfaces with a near-zero refractive index

metasurfaces enabling a wide range of refractive indices consisting of meta-atoms with the same structures may be applied to material platforms for terahertz flat optics, such as collimating lenses, focusing lenses, and refractive plates. The proposed metasurfaces would be a welcome contribution in the development of terahertz industries such as 6G wireless communications.

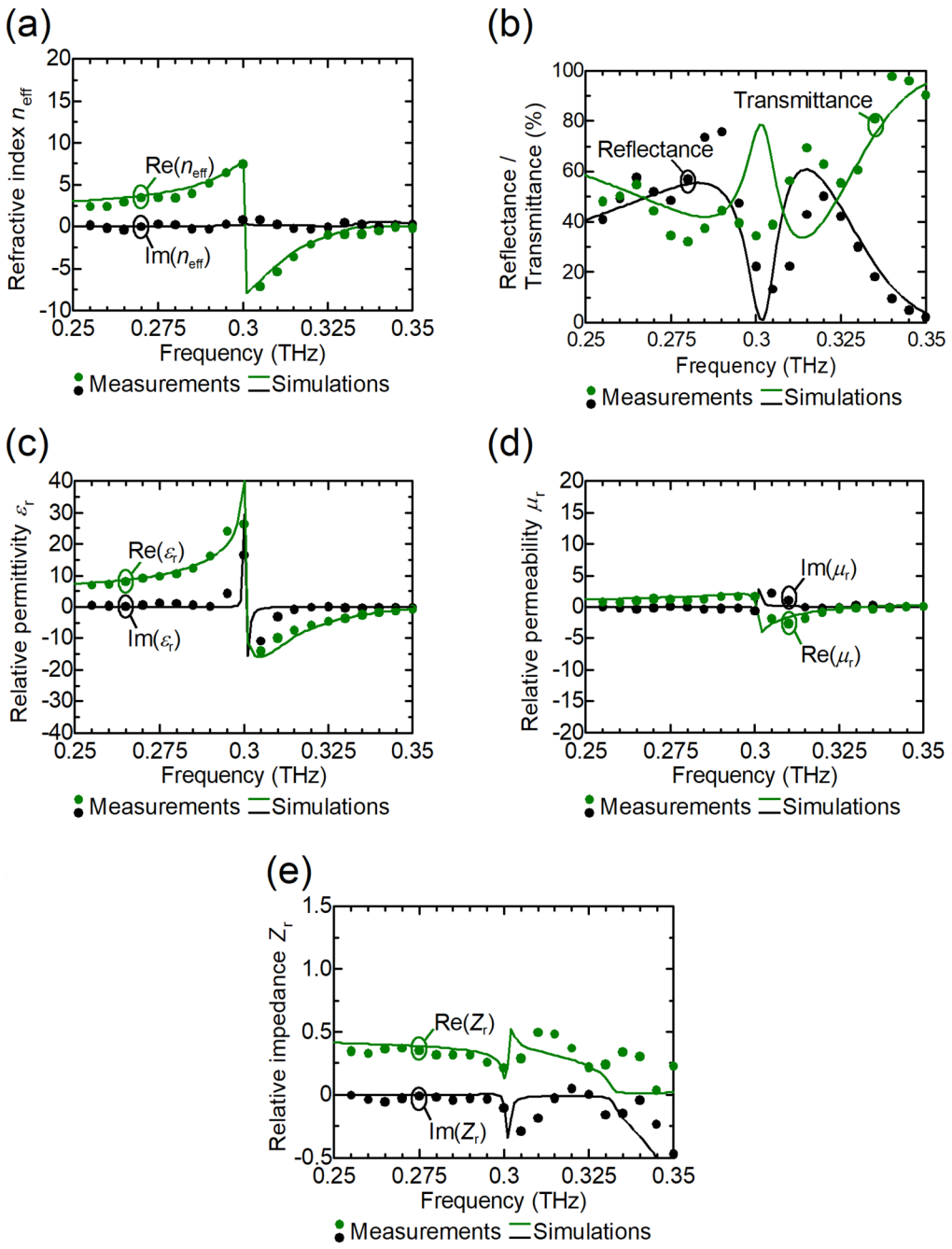


**Fig. 10** Frequency characteristics of (**a**) refractive index, (**b**) reflectance and transmittance, (**c**) relative permittivity, (**d**) relative permeability, and (**e**) relative impedance for metasurfaces with a negative refractive index

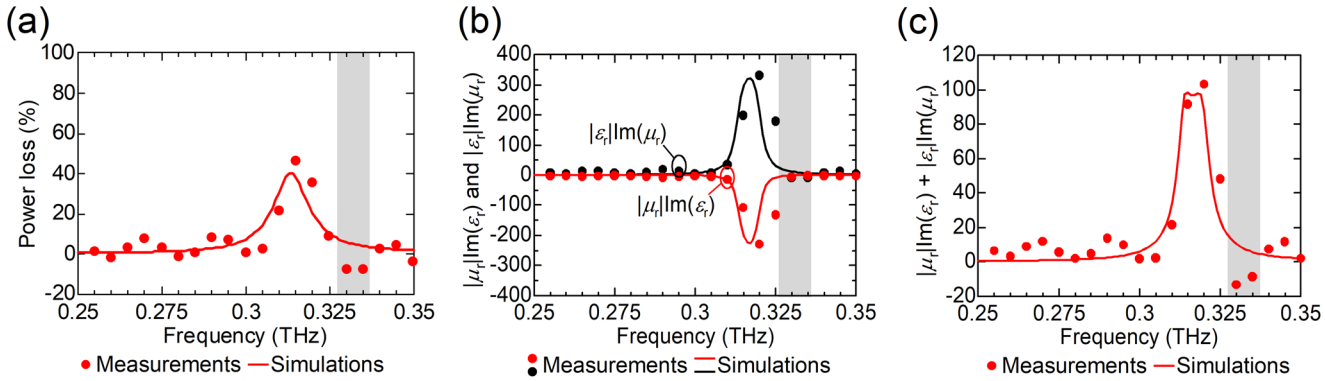


**Fig. 11** Frequency characteristics of (**a**) power loss, (**b**) dielectric energy and magnetic energy losses, and (**c**) the sum of the dielectric energy and magnetic energy losses for the metasurface with an extremely high refractive index

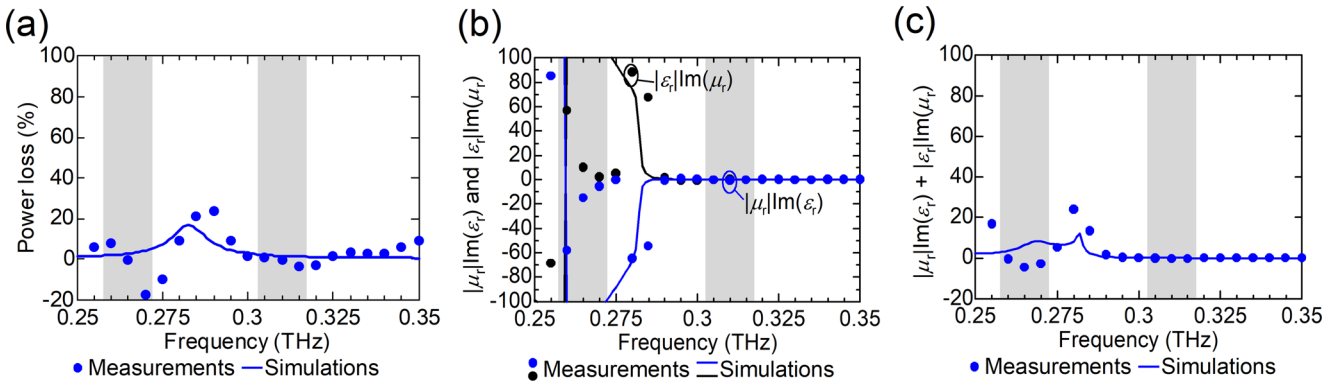


**Fig. 12** Frequency characteristics of (**a**) power loss, (**b**) dielectric energy and magnetic energy losses, and (**c**) the sum of the dielectric energy and magnetic energy losses for the metasurface with a near-zero refractive index

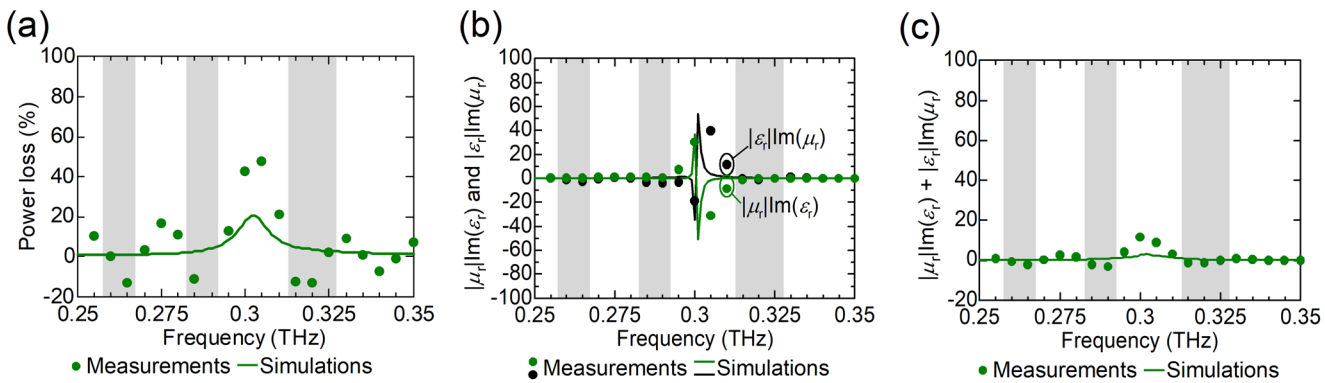


**Fig. 13** Frequency characteristics of (**a**) power loss, (**b**) dielectric energy and magnetic energy losses, and (**c**) the sum of the dielectric energy and magnetic energy losses for the metasurface with a negative refractive index

**Acknowledgements** The authors wish to thank Kaito Ebisawa and Shunji Yamamori of Tokyo University of Agriculture and Technology for the preparation of the photographs in Figs. 6(a)–(d).

**Author contributions** All authors contributed to the study conception and design. Material preparation, data collection and analysis were performed by KW, KI, RO, SK, TSa. The first draft of the manuscript was written by KS and KW, and all authors commented on previous versions of the manuscript. The research work was supervised by TSu. All authors read and approved the final manuscript.

**Funding** This research is supported by FOREST from the Japan Science and Technology Agency (JST) (JPMJFR222I), Grants-in-Aid for Scientific Research (B) from the Japan Society for the Promotion of Science (JSPS) (No. 21H01839), and Research Foundation for the Electrotechnology of Chubu.

**Data availability** Data is available upon reasonable request.

## Declarations

**Conflict of interest** The authors have no conflicts of interest to declare.

## References


1. H.-J. Song, N. Lee, Terahertz communications: challenges in the next decade. IEEE Trans. Terahertz Sci. Technol. **12**(2), 105–117 (2022). https://doi.org/10.1109/TTHZ.2021.3128677
2. H. Tataria, M. Shafi, A.F. Molisch, M. Dohler, H. Sjoland, F. Tufvesson, 6G wireless systems: vision, requirements, challenges, insights, and opportunities, Proc. IEEE 109(7), 1166–1199 (2021). https://doi.org/10.1109/JPROC.2021.3061701
3. S. Dang, O. Amin, B. Shihada, M.-S. Alouini, What should 6G be? Nat. Electron. **3**, 20–29 (2020). https://doi.org/10.1038/s41928-019-0355-6
4. I.F. Akyildiz, A. Kak, S. Nie, 6G and Beyond: the future of wireless communications systems. IEEE Access. **8**, 13395–134030 (2020). https://doi.org/10.1109/ACCESS.2020.3010896
5. P. Hillger, J. Grzyb, R. Jain, U.R. Pfeiffer, Terahertz imaging and sensing applications with silicon-based technologies. IEEE Trans. Terahertz Sci. Technol. **9**(1), 1–9 (2019). https://doi.org/10.1109/TTHZ.2018.2884852
6. H. Guerboukha, K. Nallappan, M. Skorobogatiy, Toward real-time terahertz imaging. Adv. Opt. Photon **10**(4). https://doi.org/10.1364/AOP.10.000843
7. D.M. Mittleman, Twenty years of terahertz imaging [Invited]. Opt. Express. **26**(8), 9417–9431 (2018). https://doi.org/10.1364/OE.26.009417
8. J. Ma, R. Shrestha, J. Adelberg, C.-Y. Yeh, Z. Hossain, E. Knightly, J.M. Jornet, D.M. Mittleman, Security and eavesdropping in terahertz wireless links. Nature. **563**, 89–93 (2018). https://doi.org/10.1038/s41586-018-0609-x
9. A.A. -Khalidi, K.H. Alharbi, J. Wang, R. Morariu, L. Wang, A. Khalid, J.M.L. Figueiredo, E. Wasige, Resonant tunneling diode terahertz sources with up to 1 mw output power in the J-band. IEEE Trans. Terahertz Sci. Technol. **10**(2), 150–157 (2020). https://doi.org/10.1109/TTHZ.2019.2959210
10. K. Fujita, S. Hayashi, A. Ito, M. Hitaka, Dougakiuchi Sub-terahertz and terahertz generation in long-wavelength quantum cascade lasers. Nanophotonics. **8**(12), 2235–2241 (2019). https://doi.org/10.1515/nanoph-2019-0238
11. A.S. Hajo, O. Yilmazoglu, A. Dadger, F. Kuppers, T. Kusserow, Reliable GaN-based THz Gunn diodes with side-contact and field-plate technologies. IEEE Access. **8**, 84116–84122 (2020). https://doi.org/10.1109/ACCESS.2020.2991309
12. M.A. -DelPino, N. Llombart, G. Chattopadhyay, C. Lee, C.J. -Kubiak, L. Jofre, I. Mehdi, Design guidelines for a terahertz silicon micro-lens antenna. IEEE Antennas Wirel. Propag. Lett. **12**, 84–87 (2013). https://doi.org/10.1109/LAWP.2013.2240252
13. H.D. Hristov, J.M. Rodriguez, W. Grote, The grooved-dielectric Fresnel zone plate: an effective terahertz lens and antenna. Microw. Opt. Technol. Lett. **54**(6), 1343–1348 (2012). https://doi.org/10.1002/mop.26812
14. L.P. Kamburov, J.M. Rodriguez, J.R. Urumov, H.D. Hristov, Millimeter-wave conical fresnel zone lens of flat dielectric rings. IEEE Trans. Antennas Propag. **62**(4), 2140–2148 (2014). https://doi.org/10.1109/TAP.2014.2303165
15. F. Formaneka, M.-A. Brun, T. Umetsu, S. Omori, A. Yasuda, Aspheric silicon lenses for terahertz photoconductive antennas. Appl. Phys. Express. **94**, 02113 (2009). https://doi.org/10.1063/1.3072357
16. M. Wichmann, A.S. Mondol, N. Kocic, S. Lippert, T. Probst, M. Schwerdtfeger, S. Schumann, T. Hochrein, P. Heidemeyer, M. Bastian, G. Bastian, M. Koch, Terahertz plastic compound lenses. Appl. Opt. **52**(18), 4186–4191 (2013). https://opg.optica.org/ao/abstract.cfm?uri=ao-52-18-4186
17. G.-B. Wu, Y.-S. Zeng, K.F. Chan, S.-W. Qu, C.H. Chan, 3-D printed circularly polarized modified Fresnel lens operating at terahertz frequencies. IEEE Trans. Antennas Propag. **67**(7), 4429–4437 (2019). https://doi.org/10.1109/TAP.2019.2908110
18. K. Miyamoto, K. Suizu, T. Akiba, T. Omatsu, Direct observation of the topological charge of a terahertz vortex beam generated by a Tsurupica spiral phase plate. Appl. Phys. Lett. **104**(26), 261104 (2014). https://doi.org/10.1063/1.4886407
19. Y. Yang, X. Ye, L. Niu, K. Wang, Z. Yang, J. Liu, Generating terahertz perfect optical vortex beams by diffractive elements. Opt. Express. **28**(2), 1417–1425 (2020). https://doi.org/10.1364/OE.380076
20. F. Machado, P. Zagrajek, V. Ferrando, J.A. Monsoriu, W.D. Furlan, Multiplexing THz vortex beams with a single diffractive 3-D printed lens. IEEE Trans. Terahertz Sci. Technol. **9**(1), 63–66 (2019). https://doi.org/10.1109/TTHZ.2018.2883831
21. T. Kaji, Y. Tominari, T. Yamada, S. Saito, I. Morohashi, A. Otomo, Terahertz-wave generation devices using electro-optic polymer slab waveguides and cyclo-olefin polymer clads. Opt. Express. **26**(23), 30466–30475 (2018). https://doi.org/10.1364/OE.26.030466
22. D. Grischkowsky, S. Keiding, THz time-domain spectroscopy of high tc substrates. Appl. Phys. Lett. **57**(10), 1055–1057 (1990). https://doi.org/10.1063/1.104280
23. D. Grischkowsky, S. Keiding, M. van Exter, C. Fattinger, Far-infrared time-domain spectroscopy with terahertz beams of dielectrics and semiconductors. J. Opt. Soc. Am. B **7**(10), 2006–2015 (1990). https://doi.org/10.1364/JOSAB.7.002006
24. W.T. Chen, A.Y. Zhu, F. Capasso, Flat optics with dispersion-engineered metasurfaces. Nat. Rev. Mater. **5**(8), 604–620 (2020). https://doi.org/10.1038/s41578-020-0203-3
25. N. Yu, F. Capasso, Flat optics with designer metasurfaces. Nat. Mater. **13**, 139–150 (2014). https://doi.org/10.1038/nmat3839
26. D. Lin, P. Fan, E. Hasman, M.L. Brongersma, Dielectric gradient metasurface optical elements. Science. **345**(6194), 298–302 (2014). https://doi.org/10.1126/science.1253213
27. A.V. Kildishev, A. Boltasseva, V.M. Shalaev, Planar photonics with metasurfaces. Science. **339**(6125), 1232009 (2013). https://doi.org/10.1126/science.1232009
28. N. Yu, P. Genevet, M.A. Kats, F. Aieta, J.-P. Tetienne, F. Capasso, Z. Gaburro, Light propagation with phase discontinuities: generalized laws of reflection and refraction. Science. **334**(6054), 333–337 (2011). https://doi.org/10.1126/science.1210713
29. T. Suzuki, K. Endo, J. Kim, K. Tsuruda, M. Sekiya, Metalens mounted on a resonant tunneling diode for collimated and directed terahertz waves. Opt. Express. **29**(12), 18988–19000 (2021). https://doi.org/10.1364/OE.427135
30. K. Endo, M. Sekiya, J. Kim, K. Sato, T. Suzuki, Resonant tunneling diode integrated with metalens for high-directivity terahertz waves. Appl. Phys. Express. **14**(8), 082001 (2021). https://doi.org/10.35848/1882-0786/ac0678
31. J. Neu, B. Krolla, O. Paul, B. Reinhard, R. Beigang, M. Rahm, Metamaterial-based gradient index lens with strong focusing in the THz frequency range. Opt. Express. **18**(26), 27748–27757 (2010). https://doi.org/10.1364/OE.18.027748
32. X. Jiang, H. Chen, Z. Li, H. Yuan, L. Cao, Z. Luo, K. Zhang, Z. Zhang, Z. Wen, L.-. Zhu, X. Zhou, G. Liang, D. Ruan, L. Du, L. Wang, G. Chen, All-dielectric metalens for terahertz wave imaging. Opt. Express. **26**(11), 14132–14142 (2018). https://doi.org/10.1364/OE.26.014132
33. H. Nakao, S. Kondoh, T. Suzuki, Terahertz focusing metalens of reflectionless meta-atoms with negative refractive indices. Appl. Opt. **60**, 3989–3996 (2021). https://doi.org/10.1364/AO.420836
34. H. Zhang, X. Zhang, Q. Xu, C. Tian, Q. Wang, Y. Xu, Y. Li, J. Gu, Z. Tian, C. Ouyang, X. Zhang, C. Hu, J. Han, W. Zhang, High-efficiency dielectric metasurfaces for polarization-dependent terahertz wavefront manipulation. Adv. Opt. Mater. **6**(1), 170073 (2017). https://doi.org/10.1002/adom.201700773

35. C.-C. Chang, D. Headland, D. Abbott, W. Withayachumnankul, H.-T. Chen, Demonstration of a highly efficient terahertz flat lens employing tri-layer metasurfaces. Opt. Lett. **42**(9), 1867–1870 (2017). https://doi.org/10.1364/OL.42.001867
36. M.R. Tavakol, B. Rahmani, A. Khavasi, Terahertz quarter wave-plate metasurface polarizer based on arrays of graphene ribbons. IEEE Photon Technol. Lett. **31**(12), 931–934 (2019). https://doi.org/10.1109/LPT.2019.2913503
37. J. Neu, R. Beigang, M. Rahm, Metamaterial-based gradient index beam steerers for terahertz radiation. Appl. Phys. Lett. **103**(4), 041109 (2013). https://doi.org/10.1063/1.4816345
38. H. Zeng, Y. Zhang, F. Lan, S. Liang, L. Wang, T. Song, T. Zhang, Z. Shi, Z. Yang, X. Kang, X. Zhang, P. Mazumder, D.M. Mittleman, Terahertz dual-polarization beam splitter via an anisotropic matrix metasurface. IEEE Trans. Terahertz Sci. Technol. **9**(5), 491–497 (2019). https://doi.org/10.1109/TTHZ.2019.2927890
39. B. Lv, C. Ouyang, H. Zhang, Q. Xu, Y. Li, X. Zhang, Z. Tian, J. Gu, L. Liu, J. Han, W. Zhang, All-dielectric metasurface-based quad-beam splitter in the terahertz regime. IEEE Photon J. **12**(5), 1–10 (2020). https://doi.org/10.1109/JPHOT.2020.3029057
40. K. Ishihara, T. Suzuki, Metamaterial demonstrates both a high refractive index and extremely low reflection in the 0.3-THz band. J. Infrared Millim. Terahertz Waves. **38**, 1130–1139 (2017). https://doi.org/10.1007/s10762-017-0416-8
41. T. Suzuki, M. Sekiya, T. Sato, Y. Takebayashi, Negative refractive index metamaterial with high transmission, low reflection, and low loss in the terahertz waveband. Opt. Express. **26**(7), 8314–8324 (2018). https://doi.org/10.1364/OE.26.008314
42. M. Choi, S.H. Lee, Y. Kim, S.B. Kang, J. Shin, M.H. Kwak, K.-Y. Kang, Y.-H. Lee, N. Park, B. Min, A terahertz metasurfaces with unnaturally high refractive index. Nature. **470**, 369–373 (2011). https://doi.org/10.1038/nature09776
43. H.T. Yudistira, A.P. Tenggara, V.D. Nguyen, T.T. Kim, F.D. Prasetyo, C.-G. Choi, M. Choi, D. Byun, Fabrication of terahertz metamaterial with high refractive index using high-resolution electrohydrodynamic jet printing. Appl. Phys. Lett. **103**(21), 211106 (2013). https://doi.org/10.1063/1.4832197
44. S. Tan, F. Yan, L. Singh, W. Cao, N. Xu, X. Hu, R. Singh, M. Wang, W. Zhang, Terahertz metasurfaces with a high refractive index enhanced by the strong nearest neighbor coupling. Opt. Express. **23**(22), 29222–29230 (2015). https://doi.org/10.1364/OE.23.029222
45. L. Singh, R. Singh, W. Zhang, Ultra-high terahertz index in deep subwavelength coupled bi-layer free-standing flexible metamaterials. J. Appl. Phys. **121**(23), 233103 (2017). https://doi.org/10.1063/1.4985277
46. H. Asada, K. Endo, T. Suzuki, Reflectionless metasurface with high refractive index in the terahertz waveband. Opt. Express. **29**(10), 14513–14524 (2021). https://doi.org/10.1364/OE.420827
47. Q.-L. Zhang, L.-M. Si, Y. Huang, X. Lv, W. Zhu, Low-index-metamaterial for gain enhancement of planar terahertz antenna. AIP Adv. **4**(037103) (2014). https://doi.org/10.1063/1.4868384
48. T. Suzuki, H. Asada, Reflectionless zero refractive index metasurface in the terahertz waveband. Opt. Express. **28**(15), 21509–21521 (2020). https://doi.org/10.1364/OE.395223
49. M. Awad, M. Nagel, H. Kurz, Negative-index metamaterial with polymer-embedded wire-pair structures at terahertz frequencies. Opt. Lett. **33**(22), 2683–2685 (2008). https://doi.org/10.1364/OL.33.002683
50. O. Paul, C. Imhof, B. Reinhard, R. Zengerle, R. Beigang, Negative index bulk metamaterial at terahertz frequencies. Opt. Express. **16**(9), 6736–6744 (2008). https://doi.org/10.1364/OE.16.006736
51. P. Weis, O. Paul, C. Imhof, R. Beigang, M. Rahm, Strongly birefringent metamaterials as negative index terahertz wave plates. Appl. Phys. Lett. **95**(17), 171104 (2009). https://doi.org/10.1063/1.3253414
52. T.F. Gundogdu, N. Katsarakis, M. Kafesaki, R.S. Penciu, G. Konstantinidis, A. Kostopoulos, E.N. Economou, C.M. Soukoulis, Negative index short-slab pair and continuous wires metamaterials in the far infrared regime. Opt. Express. **16**(12), 9173–9180 (2008). https://doi.org/10.1364/OE.16.009173
53. H.O. Moser, J.A. Kong, L.K. Jian, H.S. Chen, G. Liu, M. Bahou, S.M.P. Kalaiselvi, S.M. Maniam, X.X. Cheng, B.I. Wu, P.D. Gu, A. Chen, S.P. Heussler, S.B. Mahmood, L. Wen, Free-standing THz electromagnetic metamaterials. Opt. Express. **16**(18), 13773–13780 (2008). https://doi.org/10.1364/OE.16.013773
54. J. Gu, J. Han, X. Lu, R. Singh, Z. Tian, Q. Xing, W. Zhang, A close-ring pair terahertz metamaterial resonating at normal incidence. Opt. Express. **17**(22), 20307–20312 (2009). https://doi.org/10.1364/OE.17.020307
55. K. Takano, Y. Yakiyama, K. Shibuya, K. Izumi, H. Miyazaki, Y. Jimba, F. Miyamaru, H. Kitahara, M. Hangyo, Fabrication and performance of TiO2-ceramic-based metamaterials for terahertz frequency range. IEEE Trans. THz Sci. Technol. **3**(6), 812–819 (2013). https://doi.org/10.1109/TTHZ.2013.2285521
56. C.-L. Chang, W.-C. Wang, H.-R. Lin, F.J. Hsieh, Y.-B. Pun, C.-H. Chan, Tunable terahertz fishnet metamaterial. Appl. Phys. Lett. **102**, 151903 (2013). https://doi.org/10.1063/1.4801648
57. K. Watai, K. Ishihara, S. Kondoh, T. Sato, M. Shijo, T. Suzuki, Terahertz Metamaterial to Demonstrate Extremely Wide Range of Effective Refractive Indices in the 0.3-THz Band, in IEEE International Symposium on Antennas and Propagation and USNC-URSI Radio Science Meeting (2017), paper TH–A5.1A.10
58. K. Sato, T. Suzuki, Polarization-independent isotropic metasurface with high refractive index, low reflectance, and high transmittance in the 0.3-THz band. Nanophotonics. **12**(13), 2537–2544 (2023). https://doi.org/10.1515/nanoph-2022-0788
59. X. Chen, T.M. Grzegorezyk, B.-I. Wu, J. Jr. Pacheco, J.A. Kong, Robust method to retrieve the constitutive effective parameters of metamaterials. Phys. Rev. E. **70**, 016608 (2014). https://doi.org/10.1103/PhysRevE.70.016608
60. Y. Kishi, M. Nagai, J.C. Young, K. Takano, M. Hangyo, T. Suzuki, Terahertz laminated-structure polarizer with high extinction ratio and transmission power. Appl. Phys. Express. **8**(3), 032201–032201 (2015). https://doi.org/10.7567/APEX.8.032201
61. Y. Minowa, T. Fujii, M. Nagai, T. Ochiai, K. Sakoda, K. Hirano, K. Tanaka, Evaluation of effective electric permittivity and magnetic permeability in metamaterial slabs by terahertz time-domain spectroscopy. Opt. Express. **16**(7), 4785–4796 (2008). https://doi.org/10.1364/OE.16.004785


**Publisher's Note** Springer Nature remains neutral with regard to jurisdictional claims in published maps and institutional affiliations.

Springer Nature or its licensor (e.g. a society or other partner) holds exclusive rights to this article under a publishing agreement with the author(s) or other rightsholder(s); author self-archiving of the accepted manuscript version of this article is solely governed by the terms of such publishing agreement and applicable law.